David M. J. Dykstra
Institute of Physics,
Faculty of Science,
University of Amsterdam,
Amsterdam 1098 XH, Netherlands
e-mail: d.m.j.dykstra@uva.nl

Joris Busink
Institute of Physics,
Faculty of Science,
University of Amsterdam,
Amsterdam 1098 XH, Netherlands
e-mail: joris.busink@student.uva.nl

Bernard Ennis
Materials Design Department,
Tata Steel Europe R&D,
Ijmuiden 1970 CA, Netherlands
e-mail: bernard.ennis@tatasteeleurope.com

Corentin Coulais
Institute of Physics,
Faculty of Science,
University of Amsterdam,
Amsterdam 1098 XH, Netherlands
e-mail: coulais@uva.nl

Viscoelastic Snapping Metamaterials

Mechanical metamaterials are artificial composites with tunable advanced mechanical properties. Particularly, interesting types of mechanical metamaterials are flexible metamaterials, which harness internal rotations and instabilities to exhibit programable deformations. However, to date, such materials have mostly been considered using nearly purely elastic constituents such as neo-Hookean rubbers. Here, we experimentally explore the mechanical snap-through response of metamaterials that are made of constituents that exhibit large viscoelastic relaxation effects, encountered in the vast majority of rubbers, in particular, in 3D printed rubbers. We show that they exhibit a very strong sensitivity to the loading rate. In particular, the mechanical instability is strongly affected beyond a certain loading rate. We rationalize our findings with a compliant mechanism model augmented with viscoelastic interactions, which qualitatively captures well the reported behavior, suggesting that the sensitivity to the loading rate stems from the nonlinear and inhomogeneous deformation rate, provoked by internal rotations. Our findings bring a novel understanding of metamaterials in the dynamical regime and open up avenues for the use of metamaterials for dynamical shape-changing as well as vibration and impact damping applications. [DOI: 10.1115/1.4044036]

1 Introduction

Mechanical metamaterials exhibit a plethora of exotic mechanical responses. Static responses of interest span a wide range of tunable behaviors, such as auxetic [1–3], programable [4,5], shape-changing [6,7], and nonreciprocal [8] to chiral responses [9], often by harnessing nonlinear mechanics and snap-through instabilities [4,5,10–12]. Interesting dynamical responses include shock absorption [13–16], soliton propagation [17,18], and transition waves [19,20]. Importantly, a compliant mechanism framework [4,6,8,10,17–22] is often employed to capture qualitatively the mechanical response and to explore the design space.

However, the effect of the constitutive materials' dissipation has been largely overlooked for nonlinear metamaterials so far. As a matter of fact, extensive care has often been devoted in the constitutive materials' choice to avoid strong dissipative effects. Viscoelastic effects have been considered in dynamic regimes but mainly for linear metamaterials [23,24] and single snap-through elements [25,26].

Here, we investigate the role of dissipation in nonlinear snap-through metamaterials. Specifically, we probe how the constitutive materials' viscoelasticity—described by the relative stress relaxation strength and timescale, explained in Sec. 3—influences the response of a metamaterial that had been demonstrated earlier to exhibit a programable hysteric response at slow loading rate when produced from a nearly ideal elastic rubber [4,5]. We focus on metamaterials consisting of a 5×5 alternating square pattern of circular holes, as seen in Figs. 1(*a*) and 1(*b*), which have been analyzed previously in the quasistatic regime using a near ideally elastic material at low strain rates [4,5]. It was found that when such samples were confined laterally, as shown in Figs. 1(*c*) and 1(*d*), they would exhibit a snap-through response under compression, during which the central hole changes from an x-polarized state (minor diameter in the x direction) in Fig. 1(*c*) to a y-polarized state (minor diameter in the y direction) in Fig. 1(*e*), inducing a large reduction in force. During unloading, a delayed snap-back instability would occur at a lower strain level, inducing a large geometrically induced hysteresis.

However, if the sample is made instead of a viscoelastic rubber with a large stress relaxation effect and we compress the sample quickly, no pattern change is provoked in Fig. 1(*f*). This suggests a nontrivial relation between the nonlinear response—induced by the elastic instability—and dissipation—induced by viscoelasticity.

The article is structured as follows. We first describe the geometry, sample, and production process. Second, we show how we calibrate the 3D printed material using a stress relaxation test. We then present the experimental results, where we compress the sample using a variety of confinements across a wide range of strain rates, for which we systematically quantify the mechanical hysteresis and geometrical pattern change. In particular, we observe an intricate balance between the geometrically induced hysteresis and the hysteresis induced by viscoelasticity, such that optimal dissipation depends both on confinement and applied strain rate in a nontrivial manner. Finally, we present the soft viscoelastic mechanism model and its results, which we use to capture the mechanics of the interaction between viscoelasticity and mechanical instabilities.

Our study opens new avenues for the rational design of viscoelastic metamaterials, whose response drastically changes with loading rate or provides optimal energy absorption performance, combining geometrically induced hysteresis and viscous dissipation.

2 Geometry

We choose to focus exclusively on samples with 5×5 alternating holes, the smallest experimentally feasible system size, to be able to capture the essential mechanics in a simple and consistent manner. It was previously shown that the mechanics of this sample size are representative for larger metamaterials for nearly elastic samples [4,5]. The considered geometry, visualized in Fig. 1(*a*), has alternating hole sizes $D_1 = 10$ mm, $D_2 = 6$ mm, hole pitch $p = 10$ mm, local width $w = 50$ mm, height $h = 54$ mm, and thickness $t = 35$ mm. We define the biholarity, $\chi = |D_1 - D_2|/p = 0.3$. We can confine the sample laterally (in the x direction) as shown in Figs. 1(*c*) and 1(*d*), where we define the strain of confinement as $\varepsilon_x = (w_c - w)/w$, where

Contributed by the Applied Mechanics Division of ASME for publication in the Journal of Applied Mechanics. Manuscript received April 5, 2019; final manuscript received June 13, 2019; published online June 17, 2019. Assoc. Editor: Francois Barthelat.

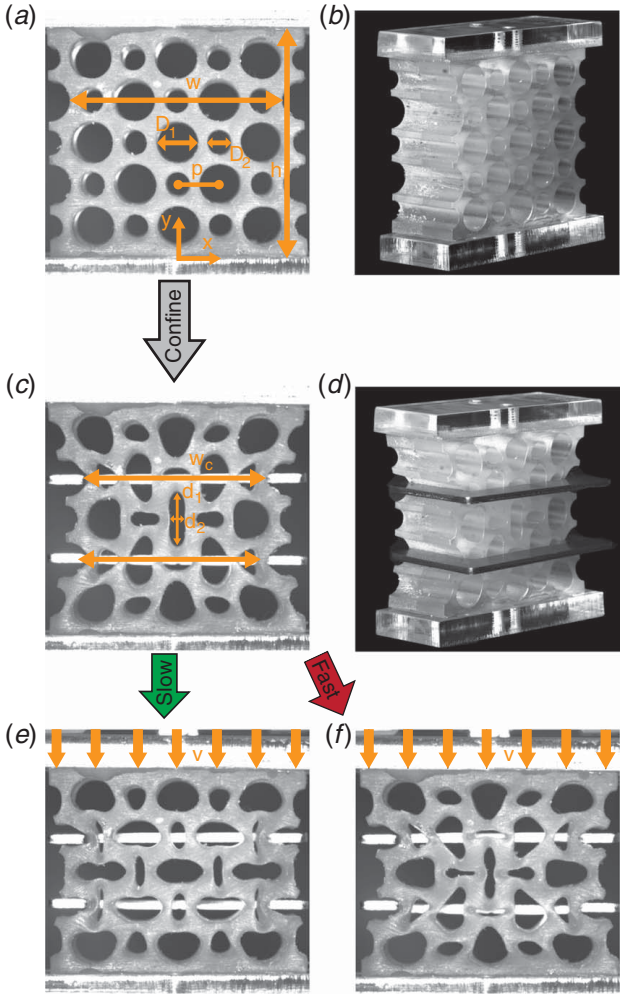

Fig. 1 (*a*) and (*b*) Picture of the metamaterial sample, with a pattern of 5 × 5 alternating holes, characterized by diameters D_1 and D_2, hole spacing p, sample height h, and local width w. (c) and (*d*) Preconfined with $\varepsilon_x = -18\%$, with the central hole initially in the x-polarized position (minor diameter in the x direction), with central hole major (d_1) and minor (d_2) axes. (*e*) Compressing slowly at a rate of $\dot{\varepsilon}_y = 9.25 \cdot 10^{-5}\,s^{-1}$ leads to a snap-through instability, changing from x- to y-polarized positions (minor diameter in the y direction). (*f*) Repeating this process fast with $\dot{\varepsilon}_y = 0.3\,s^{-1}$ suppresses the instability with the sample instead remaining in an x-polarized position.

w is the original local minimum width of the sample, seen in Fig. 1(*a*), and w_c is the same width after confinement, as shown in Fig. 1(*c*). This design is the same which was used previously for nearly elastic samples [4], for which it was demonstrated to offer a significant snap-through response for nearly elastic samples, which could be programed by modifying the level of confinement. It also allows us to compare the results from this work to previous work [4,5].

The considered geometry has been shown to have a large influence on the response for nearly elastic samples [5]. Furthermore, we expect large samples to exhibit strong size effects [4,22]. We leave interaction with alternative geometries or large samples to future work.

3 Sample Fabrication, Experimental Methods, and Calibration

We produce the sample in Fig. 1 using additive manufacturing from a rubber-like PolyJet Photopolymer (Stratasys Agilus 30) using a Stratasys Objet500 Connex3 3D printer. The flat top and bottom sides of the sample are then glued to two acrylic plates using 2k epoxy glue that allow for clamping in our uniaxial tensile tester, as performed previously [5]. To prepare the sample for testing (i) we confine the sample laterally (in the x direction) using 2 mm thick computer numerical control (CNC) machined steel U-shaped clamps as shown in Figs. 1(*c*) and 1(*d*). We choose only to confine the even rows of our sample (second and fourth), as the odd rows differ in initial width. (ii) We leave the sample unconfined. The sample is freestanding in the out-of-plane direction (z direction). The level of confinement is not affected by this direction.

The sample is compressed uniaxially, both confined and unconfined, using a uniaxial testing device (Instron 5943), which controls the vertical motion of the top side of the sample with a constant controlled velocity v as shown in Figs. 1(*e*) and 1(*f*) from $s = 0$ to $s = -12$ mm, and immediately unloaded from $s = -12$ to $s = 0$ mm at the same velocity, where we define the loading strain as $\varepsilon_y = s/h$ and strain rate as $\dot{\varepsilon}_y = |d\varepsilon_y/dt| = |v/h|$. The velocity is controlled down to ±0.1% of the set speed, while the force is monitored with a 500 N load cell with an accuracy of 0.5% down to 0.5 N. The load is balanced to F = 0 N after attaching the sample to the load cell at the top, letting the sample relax for a minute, after which the bottom is clamped to the test bench. The test is further recorded using a high resolution (2048 × 2048) grayscale CMOS camera (Basler acA2040 with Computar 75 mm lens), inducing a spatial resolution of 0.05 mm. The camera is synchronized with the uniaxial testing device, with the frame rate set such as to produce at least 400 frames per test, with exception of the highest strain rates, where the camera frame rate limits us to extract around 75 frames per test. We extract the position and ellipticity of the central hole by fitting ellipses to the images obtained using standard tessellation techniques. We calculate the polarization, Ω, of the central hole, defined as follows [4,5]:

$$\Omega = \pm(1 - d_2/d_1)\cos 2\phi \tag{1}$$

where d_1 and d_2 are the major and minor axes of the ellipse and ϕ is the angle between the major axis and the x-axis. The sign of Ω is fixed such that it is negative in an x-polarized position as in Fig. 1(*c*).

The production process results in a very viscoelastic polymer, for which we characterize the viscoelastic properties using a dogbone stress relaxation test. In a single process, we 3D printed a sample with a central slender section of Agilus 30 and comparatively rigid top and bottom sides of Stratasys VeroBlackPlus, which are used for clamping in the uniaxial testing device. The rigid sides are used to avoid prestress due to clamping. The Agilus 30 section has a length $L = 50$ mm, depth $d = 5$ mm, and width $w = 10$ mm. The sample is stretched quickly to a strain of $\varepsilon = 20\%$, similar to the global strains induced on the main sample during confinement and compression, at a strain rate of $\dot{\varepsilon} = 0.4\,s^{-1}$, after which the force is allowed to relax for 1 h. The data are measured with a frequency of 1000 Hz with $t = 0$ s defined at the point of highest load. Significant material aging effects were identified over the course of several months, which have not been fully quantified.

To describe the stress relaxation response, we assume that the instantaneous time dependent Young's modulus of the constitutive material, $E(t)$, can be modeled using a neo-Hookean material model, which can then be characterized as follows:

$$E(t) := \frac{3}{\lambda - \lambda^{-1}}\frac{F}{wd} \tag{2}$$

where λ is the applied stretch ratio and F is the measured force.

We characterize the viscoelastic properties of the constitutive material by assuming a linear Maxwell–Wiechert viscoelastic material model, containing a linear spring in parallel with a number of spring-dashpot Maxwell elements [27]. The Young's modulus' time response to a stress relaxation test is described as follows:

$$E(t) := E_0\left(1 - \sum_{n=1}^{N}\eta_n\left(1 - e^{-t/\tau_n}\right)\right) \tag{3}$$

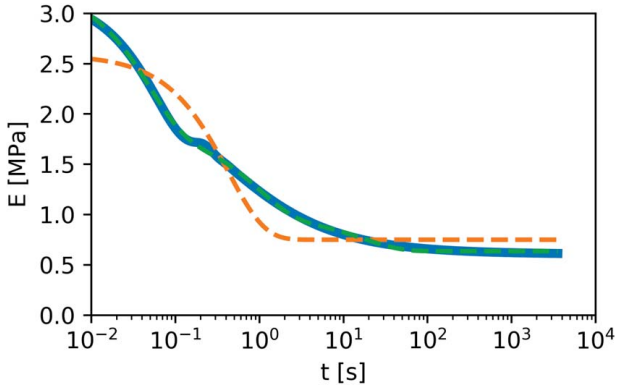

Fig. 2 Stress relaxation test results for a dogbone sample of Agilus 30 3D printed material. Instantaneous Young's modulus versus relaxation time. The thick blue line indicates the test results, and the thin dashed orange and green curves present fitted data with $N = 1$ and $N = 3$, respectively.

with E_0 the peak Young's modulus under instantaneous load, η_n the dimensionless relaxation strength, τ_n the timescale of the individual Maxwell elements [28], and N the number of Maxwell elements considered. For $N = 1$, the model reduces to the standard linear solid (SLS) model [29].

The parameters of Eq. (3) are then fitted using a least-squares fit to the test data, which was interpolated on a logarithmic time scale from 0.01 s to 1 h. The relaxation test results are presented in Fig. 2, including fits with $N = 1$ and $N = 3$ with corresponding material properties in Table 1. Very large viscoelastic effects can clearly be identified. Over the course of an hour, the effective Young's modulus drops by 80%. A single timescale is clearly insufficient to represent the material's response accurately. On the other hand, the material's response is modeled accurately using $N = 3$.

4 Experimental Results

Figure 1 shows how loading rate can change the response of the metamaterial entirely. The metamaterial in Figs. 1(*a*) and 1(*b*) is first confined laterally (Figs. 1(*c*) and 1(*d*)). When the sample in Fig. 1(*c*) is compressed slowly, with a strain rate of $\dot{\varepsilon}_y = 9.25 \cdot 10^{-5}\,\mathrm{s}^{-1}$, a pattern change appears in the central hole, going from x-polarized to y-polarized in Fig. 1(*e*), similar to what was previously observed for elastic samples [4,5]. When we repeat this process quickly, with a much higher strain rate of $\dot{\varepsilon}_y = 0.3\,\mathrm{s}^{-1}$ in Fig. 1(*f*), the response is entirely different. When compressed, viscous material dissipation induces a time delay between compression and the pattern change such that the sample remains x-polarized over the course of the compression cycle. No pattern change is observed.

In Fig. 3, we present the force–strain curves of the sample in (*a*)–(*d*), for four increasing compression rates from $\dot{\varepsilon}_y = 9.26 \cdot 10^{-5}$ to $3.09 \cdot 10^{-3}\,\mathrm{s}^{-1}$. We track the corresponding polarization in Figs. 3(*e*)–3(*h*). When loaded slowly, as shown in Figs. 3(*a*) and 3(*e*), the force–strain curves result in a large hysteresis induced by a snap-through instability similar to what was observed previously for elastic materials [4,5]. Namely, the force first increases nearly linearly, which then suddenly drops from 18 N to 6 N at a strain $\varepsilon_y = 0.1$ and then increases again until the maximum compression point. Upon decompression, the force first decreases, then snaps back up from 3 N to 6 N at a strain $\varepsilon_y = 0.05$, and finally decreases nearly linearly to zero.

Table 1 Fitted viscoelastic material properties for Agilus 30, with $N = 1$ and $N = 3$

N	E_0 (MPa)	η_1	η_2	η_3	t_1 (s)	t_2 (s)	t_3 (s)
1	2.58	0.71			0.43		
3	3.25	0.45	0.26	0.10	0.047	0.97	18

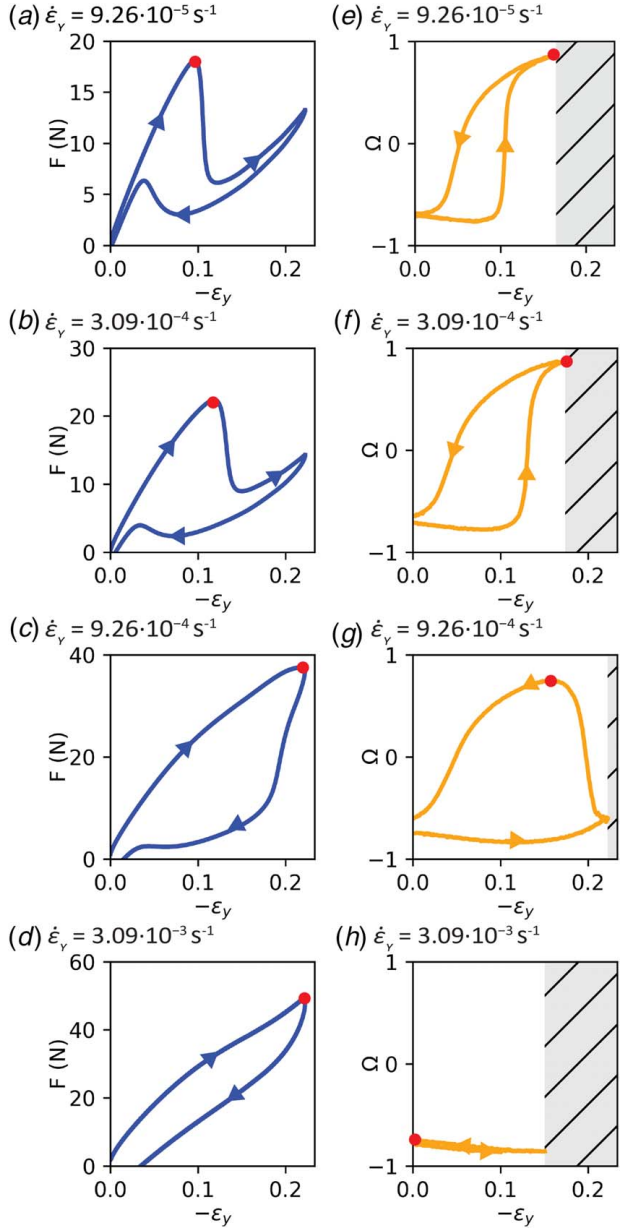

Fig. 3 Strain rate dependence of the mechanical and geometrical response of the metamaterial. (*a*)–(*d*) Force–strain response at increasing compression rates of $\dot{\varepsilon}_y = [9.26 \cdot 10^{-5}, 3.09 \cdot 10^{-4}, 9.26 \cdot 10^{-4}, 3.09 \cdot 10^{-3}]$, respectively. Red dots highlight the point of maximum force ($-\varepsilon_{yF_{max}}, F_{max}$). (*e*)–(*h*) Polarization (see text for definition) versus strain. Red dots highlight the point of maximum polarization ($-\varepsilon_{y\Omega_{max}}, \Omega_{max}$). Rastered gray areas indicate extreme polarizations which could no longer be detected, because the pore was nearly closed.

For a larger loading rate ($\dot{\varepsilon}_y = 3.09 \cdot 10^{-4}\,\mathrm{s}^{-1}$; Figs. 3(*b*) and 3(*f*)), the effects of viscoelasticity become apparent. First, the overall force scale is larger. Second, the change of polarization is delayed in Fig. 3(*f*). Accordingly, the local peak force at instability shifts to a larger strain in Fig. 3(*b*), while the peak force of snap-back during unloading shifts to a smaller strain. This leads to an increase of the relative hysteresis.

Upon faster loading ($\dot{\varepsilon}_y = 9.26 \cdot 10^{-4}\,\mathrm{s}^{-1}$), these effects are not only stronger but also the response undergoes qualitative changes

(Figs. 3(*c*) and 3(*g*)). The force scale is larger; the delay of the pattern change is increased further when loading faster still to the point where the change in polarization of the central hole is delayed to unloading instead of loading, as seen in Fig. 3(*g*). Correspondingly, no local peak force is identified anymore in Fig. 3(*c*), while the overall force scale has increased significantly due to strain rate dependent viscoelastic effects. However, the change in polarization during unloading still induces a large amount of hysteresis.

Finally, for even faster loading rates ($\dot{\varepsilon}_y = 3.09 \cdot 10^{-3}\ \mathrm{s}^{-1}$) in Figs. 3(*d*) and 3(*h*), the instability is entirely suppressed, as shown by the lack of change in the polarization of the central hole in Fig. 3(*h*). As a result, the relative hysteresis in Fig. 3(*d*) is lower than at slower loading rates, despite the fact that viscoelastic dissipation is larger.

These findings raise the question whether we can identify an optimal combination of geometrically induced and viscoelasticity-induced dissipation, depending on how fast the sample is loaded. To obtain more insight on the role of confinement and strain rate, we explore the performance of the metamaterial across a wide range of loading rates for various confinement strains in Fig. 4. In Fig. 4(*a*), we quantify the relative amount of hysteresis, H, which we define as the total percentage of energy dissipated (during both loading and unloading) with respect to the amount of work applied during the loading phase only. The strain at which we see a first local maximum force, $\varepsilon_{y,F_{\max}}$, is presented in Fig. 4(*b*). The maximum achieved polarization is given in Fig. 4(*c*). Additionally, we systematically show data for an unconfined sample that shows no instability as a benchmark (blue circles in Fig. 4).

For small strain rates ($\dot{\varepsilon}_y < 10^{-6}$), geometrically induced hysteresis dominates, where maximum clamping at $\varepsilon_x = -18\%$ implies optimal dissipation and almost no dissipation is observed for unconfined samples, as seen in Fig. 4(*a*). For the two confined cases considered here, a pattern change is induced as seen in Fig. 4(*c*). For confined samples, the accompanying mechanical instability induces a local peak force in Fig. 4(*b*).

As strain rate increases ($\dot{\varepsilon}_y \approx 10^{-5}$), as does the strain rate dependent dissipation. A general increase in relative hysteresis is seen in Fig. 4(*a*), while a delay in pattern change for confined samples shifts the local peak force to a higher strain value as seen in Fig. 4(*b*). This was also observed in the analysis of Fig. 3.

Interesting results are obtained for higher strain rates ($\dot{\varepsilon}_y \approx 10^{-4}$). No more pattern changes occur at the highest level of confinement, as can be seen by the lack of change in polarization for $\varepsilon_x = -18\%$ in Fig. 4(*c*). This removes the local snap-through peak force for $\varepsilon_x = -18\%$ in Fig. 4(*b*), which in turn leads to a decrease in relative hysteresis in Fig. 4(*a*). As such, optimal dissipation performance is now obtained for a lower level of confinement: $\varepsilon_x = -16\%$, for which the pattern change is still obtained.

As we load faster still ($\dot{\varepsilon}_y > 10^{-3}$), strain-rate-dependent dissipation takes over entirely and relative hysteresis for all two levels of confinements converge toward the response of the unconfined sample, inducing very large relative hysteresis exceeding 100% in Fig. 4(*a*), while no more pattern changes are observed for confined samples in Fig. 4(*c*). Therefore, at large strain rates, the geometrically induced instability is completely suppressed by viscoelastic effects.

These findings have been found to be very repeatable, with close to no deviation in force–strain response when measuring several cycles (not shown here).

5 Viscoelastic Compliant Mechanism

To get a better qualitative understanding of the mechanics of viscoelastic metamaterials, we enrich the soft mechanism model that was previously introduced to describe the fully elastic response [4]. The confined metamaterials can be represented by a set of rigid rectangles, connected using a set of viscoelastic torsion springs with moment M, as seen in Fig. 5(*a*), at an initial angle of $\theta_0 = \pi/4$. These rectangles are then connected to the surroundings using viscoelastic springs with an initial length of zero. Symmetry dictates that we only need to model one quarter of the mechanism, i.e., one rectangle, two linear springs, and two torsional springs. We pose that the clamps in the x direction exert a horizontal force F_1 and that the time-dependent loading in the y direction applies a force F_2. The model then contains a single degree of freedom, θ, the angle of the rectangle with respect to the horizontal. To account for viscoelastic effects, we restrict our attention to the most basic model for viscoelastic rubbers and use the SLS model [29]. These ingredients lead to the following constitutive relations:

$$F_i = u_i k\tau + u_i \eta k - \dot{F}_i \tau \tag{4}$$

$$M = 2\dot{\theta} c\tau + 2\left(\theta - \frac{\pi}{4}\right) c\eta - \dot{M}\tau \tag{5}$$

Equation (4) (Eq. (5)) applies for the linear (torsional) springs, where all torsional springs induce the same overall moment. The subscript i denotes spring 1 or 2, u is the extension of the springs, k and c are the linear and torsional peak stiffnesses under instantaneous load—comprising both elements of the SLS, in line with the definition of E_0 in Eq. (3)—ηk and ηc are the linear and torsional stiffnesses after full relaxation—comprising only the elastic part of the SLS—and the relaxation strength, $\eta = 0.8$ is considered, in line with the material stiffness drop of Fig. 2. The biholarity, $\chi = 0.3$, defined in Fig. 6 is used, similar to the experiments. All results are normalized in the time domain with respect to the viscoelastic timescale, τ. Mass is neglected because the experiments are

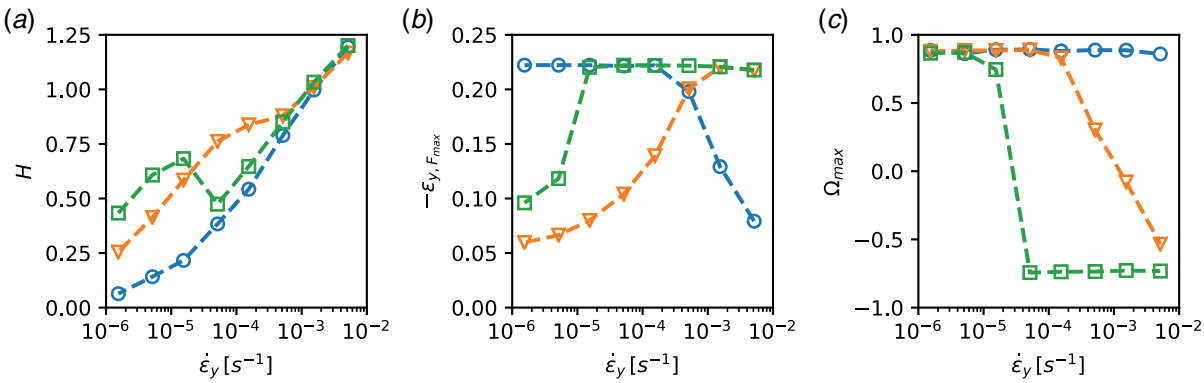

Fig. 4 Effects of confinement and loading strain rate on the response of viscoelastic metamaterials. (*a*) Percentage of hysteresis relative to the work done during loading, H versus strain rate. (*b*) Strain at which the first local maximum in force is obtained, $\varepsilon_{y,F_{\max}}$ versus strain rate. (c) Maximum polarization obtained during loading–unloading, $\Omega_{\max}$ versus strain rate. Blue circles: unconfined, orange inverted triangles: $\varepsilon_x = -16\%$, green squares: $\varepsilon_x = -18\%$.

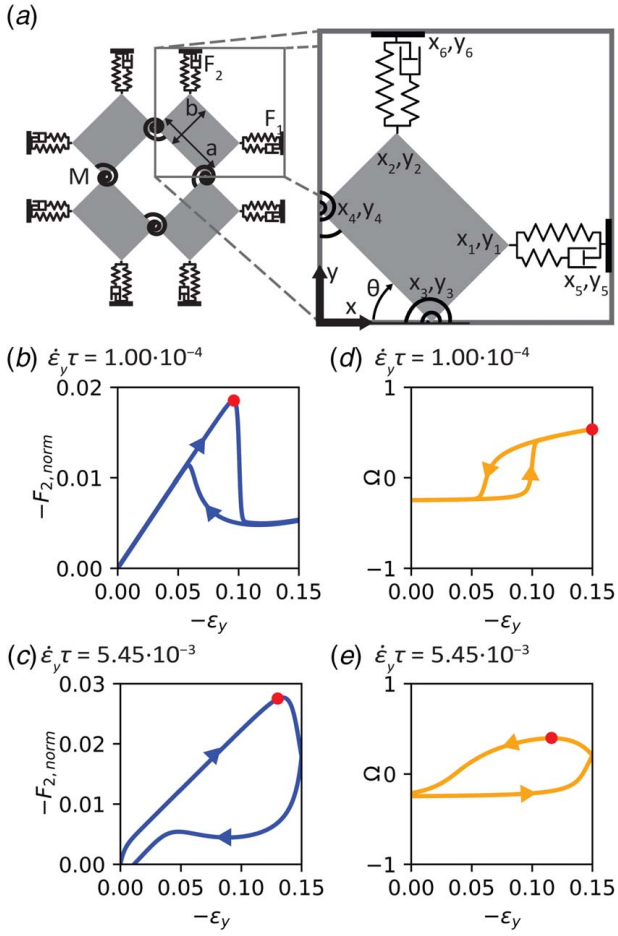

Fig. 5 Compliant viscoelastic mechanism model. (*a*) Sketch. Chosen parameters are $\chi = 2(a-b)/(a+b) = 0.3$, $\theta_0 = \pi/4$ before confinement, $\eta = 0.8$, $c = 4.2\cdot10^{-4}$ *ka*. (*b*) and (*c*) Normalized force–strain curves, with $F_{2,norm} = F_2/(kh)$, for a configuration pre-confined with $\varepsilon_x = -6.35\%$ ($\theta_1 = 53$ deg), loaded at strain rates of $\dot{\varepsilon}_y\tau = [1.0\cdot10^{-4}, 5.45\cdot10^{-3}]$, respectively. Red dots highlight the point of maximum force: $(-\varepsilon_{yF_{max}}, F_{max})$. (*d*) and (e) Corresponding polarization–strain curves. Red dots highlight the point of maximum polarization: $(-\varepsilon_{y\Omega_{max}}, \Omega_{max})$.

heavily overdamped. A torsional damper, with negligible torsional damping $\gamma = 7.5\cdot10^{-10}\cdot k/\dot{\varepsilon}_y$, is added to ensure numerical stability. We have checked that changing the value of γ by ±50% affects the force response by less than 0.1%.

From moment equilibrium, we derive the following constitutive relation:

$$\dot{\theta} = \frac{F_2(x_3 - x_2) - F_1(y_4 - y_1) - 2M}{\gamma} \tag{6}$$

where coordinates x_2, x_3, y_1, and y_4 are defined in Fig. 5(*a*).

The sides are confined with strain ε_x in the x direction, after which we can solve the relaxed equilibrium state, inducing an initial confined angle θ_1. The model of Fig. 5(*a*) can only experience a decrease in θ—and therefore a snap-through instability—during loading if $x_2 < x_3$, implying we can calculate the maximum confined angle $\theta_{1,max}$

$$\theta_{1,\,max} = \frac{\pi}{2} - \tan^{-1}\frac{b}{a} = 53.5\,\text{deg} \tag{7}$$

Similar to the experiments, we analyze the model for three cases: $\theta_1 = 53$ deg ($\varepsilon_x = -6.35\%$, large hysteresis with θ_1 just below $\theta_{1,max}$), $\theta_1 = 51$ deg ($\varepsilon_x = -4.91\%$, intermediate case with less geometric hysteresis) and $\theta_1 = 45$ deg ($\varepsilon_x = 0$, unconfined).

The mechanism is subjected to a strain field $\varepsilon_y(t)$, bilinear in the time domain, from the top, similar to what was done in the experiments. Namely, it increases linearly until full compression at a maximum applied strain of $\varepsilon_y = -0.15$ and immediately decreases linearly until zero strain. The response of the system is solved numerically in the time domain using an iterative fourth order forward Taylor series method, featuring at least 100,000 time steps, which we have checked is sufficient for numerical convergence.

For a small normalized loading rate, with $\dot{\varepsilon}_y\tau = 1.0\cdot10^{-4}$, the force–strain curve is given in Fig. 5(*b*), with the corresponding polarization in Fig. 5(*d*). Qualitatively, this response is very similar to that of Figs. 3(*a*) and 3(*e*), showing the model matches the experimental results for small quasistatic loading rates. When we increase the loading rate to $\dot{\varepsilon}_y\tau = 5.45\cdot10^{-3}$, as seen in Figs. 5(*c*) and 5(*e*) for force–strain and polarization, respectively, we see that the displacement at which we achieve maximum force shifts to higher strains, while the change in polarization is delayed such that it still increases during unloading. The behavior matches qualitatively well the experimental results of Figs. 3(*c*) and 3(*d*). Despite its limited complexity, this model can describe the experimental results well and provides illuminating physical insights on the qualitative change of response for larger loading rates as well. During the snap-through event, internal rotations of the mechanism—illustrated by Ω (Figs. 3(*d*) and 3(*e*))—are delayed by viscoelastic damping while the external strain rate remains constant. When such delay becomes longer than the timescale of the experiment, the snap-through instability is suppressed. The only behavior of Fig. 3 which cannot be described is closing of the hole before shape change at high loading rates in Figs. 3(*d*) and 3(*h*). We presume that this is due to the fact that the rectangles of Fig. 5(*a*) are considered rigid. Additional degrees of freedom, other than θ, would need to be considered to describe this behavior, which is beyond the scope of the present paper. Additionally, note that the numerical model is less confined ($\varepsilon_x = -6.35\%$) than the experimental sample ($\varepsilon_x = -18\%$) to allow for snap-through. We believe that such discrepancy possibly stems from the aforementioned simplifying assumption—wherein deformation of the rectangles is not taken into account—together with finite size effects.

Having verified that our model qualitatively matches the experiments, we can probe the model further across various loading rates and confinements (Fig. 6). Again, the obtained behavior is remarkably similar to the experiments (Fig. 4). The relative hysteresis, *H*, in Fig. 6(*a*) shows the same trend as was found in the experiments, where tight confinements induce an increase in energy absorption compared to wider confinements for small loading rates ($\dot{\varepsilon}_y\tau < 3\cdot10^{-3}$) and the values of the relative hysteresis, *H*, converge for all confinements at higher strain rates ($\dot{\varepsilon}_y\tau \approx 10^{-2}$). Additional confinement can decrease the performance in between these two regimes, as was also observed in the experiments in Fig. 4(*a*).

Figure 6(*b*) also shows results which are similar to Fig. 4(*b*) for the experiments for small loading rates ($\dot{\varepsilon}_y\tau \approx 10^{-4}$): a local peak force is found for confined samples (indicated by $-\varepsilon_{y,F_{max}} < 0.15$), which is induced at a higher strain when confinement increases from 4.91% to 6.35%. When the loading rate increases ($\dot{\varepsilon}_y\tau \approx 10^{-3}$), $-\varepsilon_{y,F_{max}}$ shifts up, which was also observed in the experiments.

Furthermore, the maximum polarization across confinements and loading rates for the numerical model is given in Fig. 6(*c*). Again, the results are qualitatively very similar to those of the experiments in Fig. 4(*c*). The main difference is that the variation of the polarization is smaller in the numerical results.

However, at high strain rates ($\dot{\varepsilon}_y\tau > 2\cdot10^{-2}$), all results of the model start to show less correspondence to the experimental results. In fact, the model predicts a decrease in dissipation instead of an increase with increased loading rate and an increase of the maximum polarization for the largest strain rates. This can be attributed to the use of a single viscoelastic timescale in the model: for very large strain rates, the viscous dissipation in the SLS model becomes irrelevant and the response becomes effectively elastic. This shows that results of the model become less valid at higher strain rates.

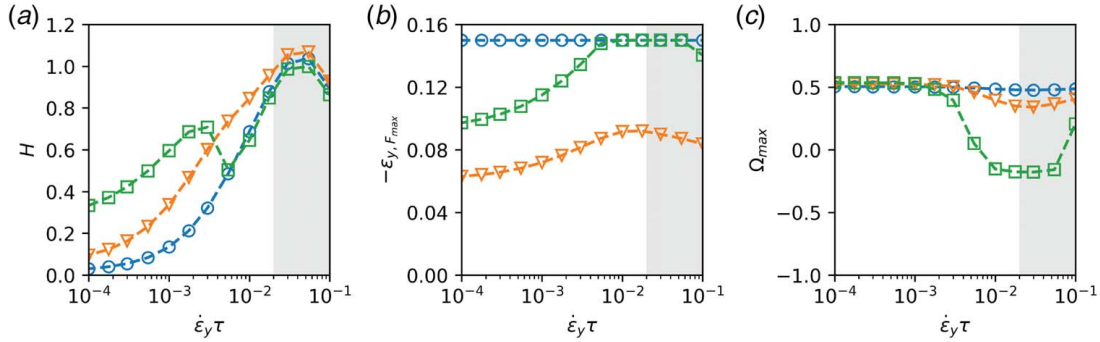

Fig. 6 Effects of confinement and loading strain rate on the response of the viscoelastic compliant mechanism. (*a*) Percentage of hysteresis relative to the work done during loading, *H* versus strain rate. (*b*) Strain at which the first local maximum in force is obtained, $\varepsilon_{y,F_{max}}$ versus strain rate. (*c*) Maximum polarization obtained during loading–unloading, Ω_{max} versus strain rate. Blue circles: no confinement ($\theta_1 = 45$ deg), orange inverted triangles: $\varepsilon_x = -4.91\%$ ($\theta_1 = 51$ deg), green squares: $\varepsilon_x = -6.35\%$ ($\theta_1 = 53$ deg). Gray areas indicate strain rates where the model is less valid.

We can also compare the equivalent timescales of the numerics and experiments. In order to bring the experimental strain rates ($\dot{\varepsilon}_y$) of Fig. 4 to the same level as the numerical normalized strain rates ($\dot{\varepsilon}_y\tau$) of Fig. 6, we need to multiply the experimental strain rates by an equivalent timescale τ_{eq}, where $1 \cdot 10^1\ \text{s} < \tau_{eq} < 3 \cdot 10^2$ s. This is in line with the longest timescale (18 s) obtained during the stress relaxation test in Table 1, providing additional validation for the model.

With the viscoelastic model validated, we use the model to probe the design space of viscoelastic metamaterials further. We focus on the influence of relaxation strength and relative torsional stiffness as follows. To do so in a consistent manner, it is important to realize that the preconfining strain necessary to trigger the instability will dramatically change with the value of the torsional stiffness. We therefore fix the relaxed confined angle $\theta_1 = 53$ deg instead, the most confined angle analyzed in Figs. 5 and 6, just below $\theta_{1,max}$. We calculate the equilibrium confinement ε_x accordingly.

In Figs. 7(*a*) and 7(*b*), we can see how the relaxation strength influences the relative hysteresis and pattern change (indicated by Ω_{max}).

For purely elastic materials ($\eta = 0$), the pattern change and obtained relative hysteresis are strain rate independent, as expected.

For moderate stress relaxation ($\eta = 0.5$), an increase in relative hysteresis is found for all strain rates, increasing with loading strain rate until results can no longer be modeled reliably ($\dot{\varepsilon}_y\tau > 2 \cdot 10^{-2}$). At $\dot{\varepsilon}_y\tau = 2 \cdot 10^{-2}$, a slight decrease in Ω_{max} is identified.

When the model becomes more viscous ($\eta = 0.8$), namely, as in the reference case analyzed above, a shift to lower strain rates is seen, where *H* and Ω_{max} are similar to those obtained with $\eta = 0.5$ when the strain rate is an order of magnitude higher. A decrease in viscoelasticity—i.e., with lower dissipation—can be countered with an increase in strain rate—i.e., with higher dissipation. A local minimum in dissipation is observed for $\eta = 0.8$ around $\dot{\varepsilon}_y\tau = 6 \cdot 10^{-3}$, which was also found in the experiments. This is in contrast with the case $\eta = 0.5$, where no such minimum occurs in the strain rate window considered here.

Energy dissipation increases significantly for materials with extremely large relaxation ($\eta = 0.99$), with $H > 1.7$ around $\dot{\varepsilon}_y\tau \approx 10^{-2}$. Another shift down in strain rate, with nearly 2 orders of magnitude, is seen with respect to $\eta = 0.8$. Interestingly, a similar local minimum in dissipation is identified for both $\eta = 0.8$ and $\eta = 0.99$ ($H \approx 0.5$ for $\dot{\varepsilon}_y\tau \approx 5 \cdot 10^{-3}$ and $\dot{\varepsilon}_y\tau \approx 10^{-4}$, respectively), corresponding to the lowest strain rates at which no more pattern change is identified. Furthermore, the geometrically induced relative hysteresis seems to present a lower limit for relative hysteresis. Any combination with relaxation strength always induces a larger relative hysteresis, regardless of whether a pattern change occurs.

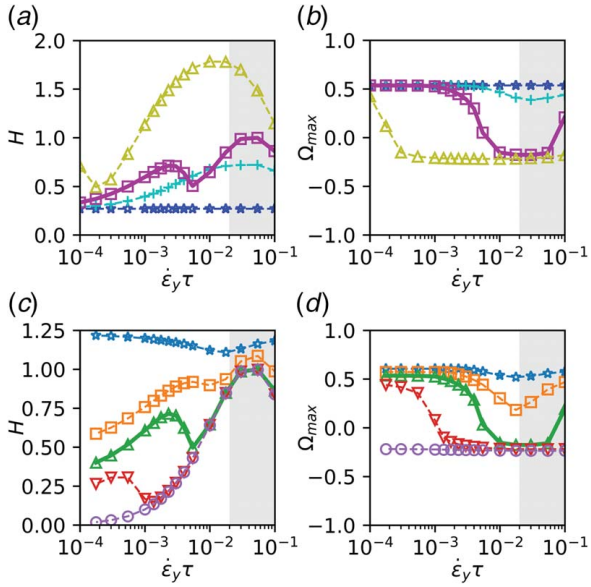

Fig. 7 Effects of stress relaxation and torsional stiffness and loading strain rate on the viscoelastic compliant mechanism. (*a*) Percentage of hysteresis relative to the work during loading, *H* versus strain rate, for varying viscosities, η. Blue stars: $\eta = 0$, cyan plus: $\eta = 0.5$, magenta squares (thick solid line, reference configuration): $\eta = 0.8$, yellow triangles: $\eta = 0.99$. (*b*) Maximum polarization obtained during loading–unloading, Ω_{max} versus strain rate, for the same cases. (*c*) Percentage of relative hysteresis *H* versus strain rate, for varying torsional stiffnesses, $\beta = c/c_{ref}$, where c_{ref} is the torsional stiffness used for Figs. 5 and 6. Blue stars: $\beta = 0$, orange squares: $\beta = 0.5$, green triangles (thick solid line, reference configuration): $\beta = 1$, red inverted triangles: $\beta = 2$, purple circles: $\beta = 4$. (*d*) Maximum polarization obtained during loading–unloading, Ω_{max} versus strain rate, for the same cases. Gray areas indicate strain rates where the model is less valid.

In a similar way, Figs. 7(*c*) and 7(*d*) show how torsional stiffness affects the relative hysteresis and pattern change (indicated by Ω_{max}) in the metamaterial. When the torsional stiffness is reduced, pattern changes can be obtained at larger strain rates. Furthermore, the elastic energy in the torsional springs during pattern change is reduced relative to the geometric hysteretic energy, inducing a higher percentage of relative hysteresis. These two effects imply an increase in relative dissipation for lower torsional stiffnesses. However, in cases without pattern change ($\beta \geq 1$, $\dot{\varepsilon}_y\tau > 10^{-2}$), the values of the relative hysteresis, *H*, converge

for all confinements. In this regime, dissipation induced by geometrical effects becomes irrelevant and viscoelastic dissipation completely dominates.

6 Discussion

In this paper, we have investigated the interaction between elastic snap-through energy dissipation and viscoelastic energy dissipation in mechanical metamaterials. To this end, we 3D printed, from a photopolymer exhibiting very large stress relaxation (80%), confined reprogramable metamaterials, for which it was previously demonstrated to exhibit an elastic hysteretic response when compressed in a quasistatic manner [4,5].

We found that viscoelasticity can change the geometric response of the metamaterial entirely under moderate to large strain rates. A pattern change resulting from a snap-through instability could be delayed or even suppressed when the metamaterial is loaded more quickly, drastically affecting the observed relative hysteresis. This qualitative change originates from the competition of the timescales of external loading—depending on external strain rate—and internal rotations—mediated by viscoelastic damping. For high strain rates, the energy dissipation is governed entirely by the inherent material dissipation, while for low strain rates, the hysteretic response reduces to the elastic quasistatic response. Strong interactions between geometry and viscoelasticity can be found for intermediate loading rates, where increased lateral confinement reduces the strain rate after which no more pattern change can be observed. As a result, wider lateral confinements, which would provide less dissipation for purely elastic samples, can provide more dissipation for certain moderate strain rates than more narrow confinements would. We also demonstrated that we can capture the behavior of these samples using a simple viscoelastic compliant mechanism model, which we use to explore the design space further. We find that the response of the viscoelastic metamaterial also depends strongly on the elastic hinges connecting the mechanism, which are stressed during the pattern change, as well as the relaxation strength of the constitutive material. Decreasing either the torsional stiffness of the hinges or the relaxation strength or the viscoelastic timescales of the constitutive material can enable dissipation enhancing pattern changes at higher strain rates. Furthermore, we demonstrate that a single viscoelastic timescale is insufficient to describe the response of these metamaterials at higher strain rates.

We therefore show that an optimal energy dissipating metamaterial is not merely a combination of the ideal geometric and viscoelastic dissipative metamaterial. Instead, for any given loading rate, the ideal combination of geometrically induced and viscoelastic dissipation should be selected, still allowing for a mechanical instability. The current metamaterial design we present allows for programing the ideal response for a given loading rate, implying in principle that we can rationally tune the shock damping performance without changing the base metamaterial.

Our findings bring a novel understanding of metamaterials in the dynamical regime and open up avenues for the use of metamaterials for vibration and impact applications, utilizing both geometrically induced and viscoelastic dissipation. Furthermore, our findings offer new perspectives for the development of new types of metamaterials which can alter their response in different dynamic situations.

An open question remains how to leverage geometric dissipation at higher strain rates such that geometrically induced dissipation can still be harnessed, while still harnessing viscous dissipation at lower strain rates, for increased performance across a range of strain rates. The next question is: how general are these results? Is the response under nonlinear vibrations or under shock—at much larger loading rates—similar? Will larger metamaterials and other geometries yield the same results, with or without mechanical snap-through? Finally, the compliant mechanism model only considers a single timescale, which was deemed insufficient at larger strain rates. Will using multiple timescales model result in more reliable results for any loading condition and are three timescales sufficient?

Acknowledgment

We thank D. Giesen, S. Koot, and G. Hardeman for their skillful technical assistance, as well as Jan Heijne at Tata Steel Europe for assistance with mechanical testing. C.C. acknowledges funding from the Netherlands Organization for Scientific Research (NWO) VENI grant no. NWO-680-47-445.

References

[1] Lakes, R., 1987, "Foam Structures With a Negative Poisson's Ratio," Science, **235**(4792), pp. 1038–1040.
[2] Bertoldi, K., Reis, P. M., Willshaw, S., and Mullin, T., 2010, "Negative Poisson's Ratio Behavior Induced by an Elastic Instability," Adv. Mater., **22**(3), pp. 361–366.
[3] Babaee, S., Shim, J., Weaver, J. C., Chen, E. R., Patel, N., and Bertoldi, K., 2013, "3D Soft Metamaterials With Negative Poisson's Ratio," Adv. Mater., **25**(36), pp. 5044–5049.
[4] Florijn, B., Coulais, C., and van Hecke, M., 2014, "Programmable Mechanical Metamaterials," Phys. Rev. Lett., **113**(17), p. 175503.
[5] Florijn, B., Coulais, C., and van Hecke, M., 2016, "Programmable Mechanical Metamaterials: The Role of Geometry," Soft Matter, **12**(42), pp. 8736–8743.
[6] Overvelde, J. T. B., Weaver, J. C., Hoberman, C., and Bertoldi, K., 2017, "Rational Design of Reconfigurable Prismatic Architected Materials," Nature, **541**(7637), pp. 347–352.
[7] Coulais, C., Sabbadini, A., Vink, F., and van Hecke, M., 2018, "Multi-Step Self-Guided Pathways for Shape-Changing Metamaterials," Nature, **561**(7724), pp. 512–515.
[8] Coulais, C., Sounas, D., and Alù, A., 2017, "Static Non-Reciprocity in Mechanical Metamaterials," Nature, **542**(7642), pp. 461–464.
[9] Frenzel, T., Kadic, M., and Wegener, M., 2017, "Three-Dimensional Mechanical Metamaterials With a Twist," Science, **358**(6366), pp. 1072–1074.
[10] Rafsanjani, A., and Pasini, D., 2016, "Bistable Auxetic Mechanical Metamaterials Inspired by Ancient Geometric Motifs," Extreme Mech. Lett., **9**(2), pp. 291–296.
[11] Che, K., Yuan, C., Wu, J., Qi, H., and Meaud, J., 2017, "Three-Dimensional-Printed Multistable Mechanical Metamaterials With a Deterministic Deformation Sequence," ASME J. Appl. Mech., **84**(1), p. 011004.
[12] Restrepo, D., Mankame, N. D., and Zavattieri, P. D., 2015, "Phase Transforming Cellular Materials," Extreme Mech. Lett., **4**, pp. 52–60.
[13] Frenzel, T., Findeisen, C., Kadic, M., Gumbsch, P., and Wegener, M., 2016, "Tailored Buckling Microlattices as Reusable Light-Weight Shock Absorbers," Adv. Mater., **28**(28), pp. 5865–5870.
[14] Shan, S., Kang, S. H., Raney, J. R., Wang, P., Fang, L., Candido, F., Lewis, J. A., and Bertoldi, K., 2015, "Multistable Architected Materials for Trapping Elastic Strain Energy," Adv. Mater., **27**(29), pp. 4296–4301.
[15] Correa, D. M., Klatt, T., Cortes, S., Haberman, M., Kovar, D., and Seepersad, C., 2015, "Negative Stiffness Honeycombs for Recoverable Shock Isolation," Rapid Prototyping J., **21**(2), pp. 193–200.
[16] Schaedler, T. A., Ro, C. J., Sorensen, A. E., Eckel, Z., Yang, S. S., Carter, W. B., and Jacobsen, A. J., 2014, "Designing Metallic Microlattices for Energy Absorber Applications," Adv. Eng. Mater., **16**(3), pp. 276–283.
[17] Deng, B., Raney, J. R., Tournat, V., and Bertoldi, K., 2017, "Elastic Vector Solitons in Soft Architected Materials," Phys. Rev. Lett., **118**(20), p. 204102.
[18] Deng, B., He, P. W. Q., Tournat, V., and Bertoldi, K., 2018, "Metamaterials With Amplitude Gaps for Elastic Solitons," Nat. Commun., **9**(1), p. 3410.
[19] Raney, J. R., Nadkarni, N., Daraio, C., Kochmann, D. M., Lewis, J. A., and Bertoldi, K., 2016, "Stable Propagation of Mechanical Signals in Soft Media Using Stored Elastic Energy," Proc. Natl. Acad. Sci. U.S.A., **113**(35), pp. 9722–9727.
[20] Nadkarni, N., Arrieta, A. F., Chong, C., Kochmann, D. M., and Daraio, C., 2016, "Unidirectional Transition Waves in Bistable Lattices," Phys. Rev. Lett., **116**(24), p. 244501.
[21] Coulais, C., 2016, "Periodic Cellular Materials With Nonlinear Elastic Homogenized Stress-Strain Response at Small Strains," Int. J. Solids Struct., **97–98**, pp. 226–238.
[22] Coulais, C., Kettenis, C., and van Hecke, M., 2017, "A Characteristic Length-Scale Causes Anomalous Size Effects and Boundary Programmability in Mechanical Metamaterials," Nat. Phys., **14**(1), pp. 40–44.
[23] Wang, A., Shang, J., Li, X., Luo, Z., and Wu, W., 2018, "Vibration and Damping Characteristics of 3D Printed Kagome Lattice With Viscoelastic Material Filling," Sci. Rep., **8**(1), p. 9604.
[24] Parnell, W. J., and De Pascalis, R., 2019, "Soft Metamaterials With Dynamic Viscoelastic Functionality Tuned by Pre-Deformation," Philos. Trans. R. Soc. A, **377**(2144), p. 20180072.
[25] Gomez, M., Moulton, D. E., and Vella, D., 2019, "Dynamics of Viscoelastic Snap-Through," J. Mech. Phys., **124**, pp. 781–813.
[26] Arrieta, A. F., Wagg, D. J., and Neild, S. A., 2011, "Dynamic Snap-Through for Morphing of Bi-Stable Composite Plates," J. Intell. Mater. Syst. Struct., **22**(2), pp. 103–112.
[27] Wiechert, E., 1893, "Gesetze Der Elastischen Nachwirkung Für Constante Temperatur," Ann. Phys., **286**(11), pp. 546–570.
[28] Christensen, R., 2003, *Theory of Viscoelasticity*, 2nd ed., Dover Publications Inc., New York.
[29] Lakes, R., 2009, *Viscoelastic Materials*, Cambridge University Press, Cambridge.